

Intrinsic origin and enhancement of topological responses in ferrimagnetic antiperovskite Mn₄NTemujin Bayaraa^{1,2,*}, Vsevolod Ivanov^{1,3}, Liang Z. Tan,² and Sinéad M. Griffin^{1,2}¹*Materials Sciences Division, Lawrence Berkeley National Laboratory, Berkeley, California 94720, USA*²*Molecular Foundry Division, Lawrence Berkeley National Laboratory, Berkeley, California 94720, USA*³*Accelerator Technology and Applied Physics Division, Lawrence Berkeley National Laboratory, Berkeley, California 94720, USA*

(Received 13 April 2023; revised 16 August 2023; accepted 19 December 2023; published 29 January 2024)

Using first-principles calculations we investigate the intrinsic origins of the anomalous Hall effect (AHE) and the anomalous Nernst effect (ANE) in antiperovskite ferrimagnet Mn₄N. We predict that the AHE is significantly enhanced under both compressive and tensile strain; however, the ANE generally decreases under epitaxial strain, except for 1% compressive strain. We connect this behavior to the evolution of the Berry curvature with strain, suggesting similar strategies for achieving large AHE and ANE changes with modest amounts of strain. Finally, we find that the nonmonotonic characteristics of the AHE and ANE stem from the formation and movement of new Weyl points at the periphery of the Brillouin zone under compressive and tensile strains.

DOI: [10.1103/PhysRevB.109.014430](https://doi.org/10.1103/PhysRevB.109.014430)**I. INTRODUCTION**

The application of topology in condensed matter physics has become widely embraced and has renewed our understanding of electronic band structures of materials [1–3]. This framework enables the understanding of symmetry-protected features in reciprocal space found in topological insulators and semimetals. Combining nontrivial topology with time-reversal symmetry breaking can lead to large Berry curvatures that enable sizable macroscopic responses such as the anomalous Hall effect (AHE) and the related anomalous Nernst effect (ANE) with great potential applications ranging from thermoelectrics to spin-based storage [4,5]. In fact, the key step to understanding the intrinsic origins of the AHE was in identifying the relationship between the AHE and the Berry curvature of the occupied electronic bands in a crystal [6].

Antiperovskite transition-metal nitrides, especially Mn₄N, have a diverse range of magnetic properties and emergent phases, which make them interesting for both understanding fundamental physics and for spin-based applications. Mn₄N has a high Néel temperature ($T_N = 745$ K), small saturation magnetization, and high uniaxial magnetic anisotropy, making it particularly appealing for thermoelectric applications based on the ANE [7–24]. Mn₄N is also predicted to host a wealth of real-space magnetic topological features including spin textures, hedgehog-antihedgehog pairs and skyrmion tubes [18,25,26]. These nontrivial spin structures were found to be mainly stabilized by the frustration induced by the magnetic exchange interaction between fourth-nearest neighbors [27]. More recently, measurements of the AHE and ANE were reported for Mn₄N [17,18,21–24,28]; however, they do not agree on the origin of the AHE in Mn₄N, and importantly, do not address how it can be enhanced through experimentally viable routes such as strain. In particular, the microscopic

origins of the AHE can either be extrinsic (e.g., due to spin-orbit induced scattering) or intrinsic (related to the Berry curvature). Recent experimental work studied transport signatures of the AHE in epitaxial Mn₄N films of different thickness, and concluded that the AHE has competing contributions from skew scattering, side jump, and intrinsic mechanisms [21]. According to the conventional scaling law $\rho_{\text{AHE}} \propto \rho_{xx}^\gamma$ [6], where ρ_{AHE} is anomalous Hall resistivity and ρ_{xx}^γ is longitudinal resistivity, γ was found to be larger than 2 for all Mn₄N films, indicating that the side jump and intrinsic mechanisms are dominant in these films [29,30]. On the other hand, Isogami *et al.* [17] report a dominant intrinsic contribution to AHE and ANE based on transport and *ab initio* calculations.

Surprisingly, we are not aware of a comprehensive study of the electronic origins of the AHE and ANE from the perspective of first-principles-based calculations, or nor a discussion of how these properties can be enhanced. Moreover, the range of competing, frustrated magnetic states in ferrimagnetic Mn₄N motivates us to explore the range of tunability of the topological responses in this system.

The antiperovskite structure of Mn₄N can be viewed as Mn₃MnN with Mn ions on three inequivalent cation sublattices and N taking the anion site [Fig. 1(a)]. These three different Mn sublattices have unequal magnetic moments leading to its ferrimagnetic nature and small saturation magnetization. Neutron diffraction experiments identified two different magnetic configurations in Mn₄N [31]. In the “type-A” structure, the spins of Mn II and Mn III are aligned parallel to each other but antiparallel to those of Mn I, whereas in the “type-B” structure, the spins of Mn I and Mn II are aligned parallel to each other while being antiparallel to the spins of Mn III [see Fig. 1(a)] [11,17,27]. Previous theoretical works found the type-B to be the ground state, although both have been observed in experiment [17]. We find the type-B configuration to have 272 meV/f.u. lower in energy than the type-A configuration, motivating our focus on type-B for the main analysis of the paper (see the Supplemental Material [32] for the comparison between type-A and type-B configurations). Note that

*tbayaraa@lbl.gov

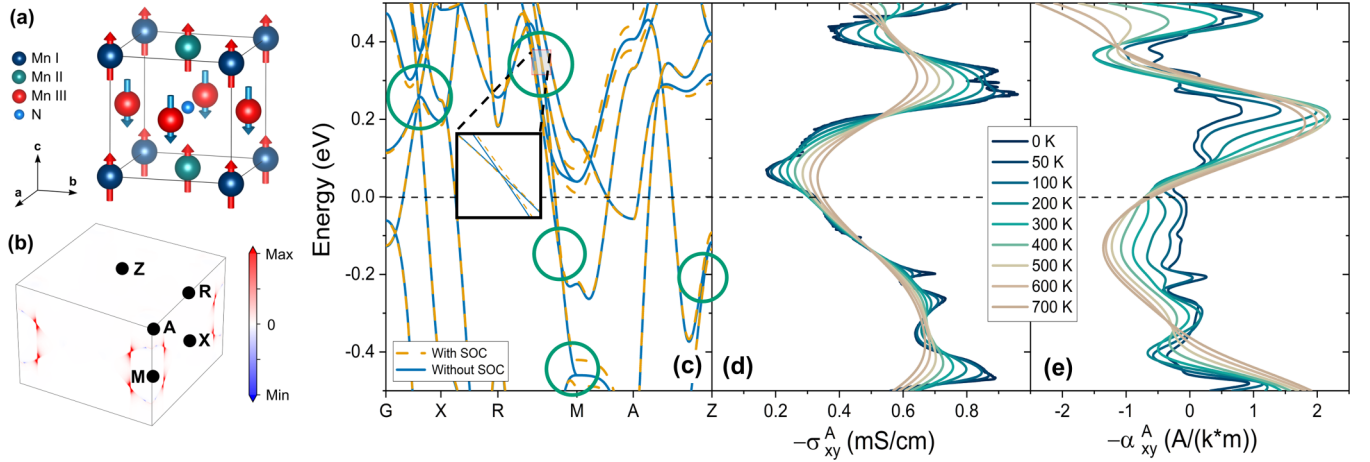


FIG. 1. The crystal structure of Mn₄N with type-B magnetic structure indicated with arrows (a), and the calculated Berry curvature Ω_z distribution in the BZ (b). Black dots represent the high-symmetry points in the BZ and only most robust Berry curvature distributions are shown. Calculated band structure with and without spin-orbit coupling (c), calculated anomalous Hall conductivity σ_{xy}^A (d), and anomalous Nernst conductivity α_{xy}^A (e), as a function of a total energy with respect to the Fermi energy. Note that green circles show the possible band crossings that corresponds to the peaks in anomalous Hall effect. The Fermi level is marked by the dashed line. The inset shows a zoomed-in region of the band crossings where one can see SOC inducing band openings.

noncollinear spin configurations were also observed in the Mn₄N system [33,34]; however, they were found to be energetically less favorable than the collinear spin configurations.

II. COMPUTATIONAL DETAILS

All first-principles calculations were carried out within the framework of density functional theory (DFT) as implemented in Vienna *Ab Initio* Software Package (VASP) [35] using the projector augmented-wave potentials [36]. We used the generalized gradient approximation, with the Perdew-Burke-Ernzerhof exchange-correlation functional [37,38], and an effective Hubbard U parameter of 0.54 eV for the localized 3d electrons of the Mn ions (see Supplemental Material [32] for more info). We selected this Hubbard U value so that the lattice parameters were close to those reported in experiment for the type-B magnetic structure. In particular, we calculated the in-plane lattice constant, $a_{ip} = 3.897 \text{ \AA}$ ($a_{ip} = 3.89 \text{ \AA}$ in experiment [31]) and the c/a axial ratio = 0.98 (≈ 0.99 in experiment [31]). All calculations were performed with the type-B magnetic structure for which we found the calculated magnetic moments to be $3.6 \mu_B$, $1.16 \mu_B$, and $-3.01 \mu_B$ for Mn I, Mn II, and Mn III, respectively. We used an energy cutoff of 800 eV and a Monkhorst-Pack k -point mesh density of $13 \times 13 \times 13$ for Brillouin zone (BZ) sampling. All structural relaxations were performed until the Hellmann-Feynman force on each atom is less than 0.001 eV/\AA . For the bulk case, we allowed all structural degrees of freedom to optimize (lattice parameters and internal coordinates); however, for the epitaxial strain calculations, we fixed the in-plane (001) lattice vectors and allowed the out-of-plane lattice vector and atomic positions to relax. All calculations included spin-orbit coupling (SOC) self consistently as implemented in VASP.

From the Bloch states obtained in the DFT calculation described above, we constructed a Wannier-based tight-binding

model [39], which we then used to calculate the intrinsic AHC (σ_{ij}^A) and ANE (α_{ij}^A) as proposed by Xiao *et al.* [40],

$$\sigma_{ij}^A = -\frac{e^2}{\hbar} \sum_n \int \frac{dk}{(2\pi)^3} \Omega_{n,ij} f_n(T), \quad (1)$$

$$\alpha_{ij}^A = -\frac{e}{T\hbar} \sum_n \int \frac{dk}{(2\pi)^3} \Omega_{n,ij} \left\{ (E_n - E_F) f_n(T) + k_B T \ln\left(1 + e^{\frac{E_n - E_F}{-k_B T}}\right) \right\}, \quad (2)$$

where e is the elementary charge, \hbar the reduced Planck constant, $\Omega_{n,ij}$ the Berry curvature, f_n the Fermi-Dirac distribution function with the band index n and the wave vector \mathbf{k} , k_B the Boltzmann constant, E_n the band energy, and E_F the Fermi level. We used a $501 \times 501 \times 501$ mesh for integrations over BZ to calculate the AHE and ANE in Wannier tools [41]. Note that this mesh was carefully checked to ensure convergence.

III. BULK TOPOLOGICAL RESPONSES

We first focus on the calculated electronic topological properties of bulk Mn₄N. Figure 1(c) shows the calculated band structure with and without SOC between the high-symmetry points in the BZ. Note that the magnetic space group of Mn₄N is $P4/mmm'$ with its magnetic easy axis along the out-of-plane z direction [42]. We find multiple band crossings without SOC that are gapped out with the inclusion of SOC, for instance along the R-M line. We identify these as the source of Berry curvature Ω by explicit calculation of the Berry curvature where we plot its dominant component Ω_z in Fig. 1(b). While there can be many different sources of Ω , a strong contribution can originate from Weyl points (WP) that act as like a monopoles for Ω , or from nodal lines that are gapped out when a mirror symmetry is broken via magnetization. We identify the WPs that contribute most to

the Berry curvature using Wannier tools [41], and show them in the Supplemental Material [32].

Since such peaks in Berry curvature are an intrinsic source of the AHE (and ANE), we next report the calculated anomalous Hall conductivity (AHC) and anomalous Nernst conductivity (ANC) as functions of energy with respect to the Fermi level at temperatures ranging from 0 K to 700 K [Figs. 1(d) and 1(e)]. (Note that the Néel temperature of bulk Mn_4N is 745 K [12]. Since only the Ω_Z component of the Berry curvature is nonzero due to symmetry, we show the transverse (xy) component of the AHC (σ_{xy}^A) and the ANE (α_{xy}^A), focusing on an energy range surrounding the Fermi level as this will determine the measured transport responses. We find that the band structure has several crossings above and below Fermi level that result in large Berry curvatures, leading to multiple peaks in the AHE shown in Fig. 1(d). Here, we focus on the dominant peak at $E \sim +0.3$ eV, which corresponds to the band crossings shown in Fig. 1(c). The AHE peak at $E \sim +0.3$ eV becomes sharper as the system cools down and eventually splits into two peaks at $E \sim +0.28$ eV and $+0.32$ eV at $T = 0$ K, corresponding to the band crossings identified in the 0 K band structure in Fig. 1(c). On the other hand, we find that at high temperatures the ANE [Fig. 1(e)] is peaked at $E \sim +0.2$ eV and $\sim +0.4$ eV but with opposite signs in this energy range close to the Fermi level. This is consistent with our calculated AHE peak at $E \sim +0.3$ eV since the thermoelectric conductivity α_{ij}^A is proportional to the energy derivative of the AHE at low temperatures, which is known as the Mott relation. We note that the ANE signal at the Fermi level and the peak at $E \sim +0.2$ eV both reach their maximum values around 400 K, dropping for higher temperatures. This is in contrast to the overall increase in thermoelectric conductivity with temperature, which reaches its maximum at 700 K for other energy ranges. This feature may be explained by considering the previous prediction of the magnetization compensation temperature (~ 500 K) in this system [27]. However, we also note a sign reversal in the thermoelectric conductivity with increasing temperature at $E \sim +0.4$ eV. While this is far enough away from the Fermi level in stoichiometric films to not influence transport, it could play a role in doped or alloyed systems [43–46].

We calculate the AHC, σ_{xy}^A , to be -323 S/cm at the Fermi level and at 0 K, which is three times larger than the experimental result of -100 S/cm at 4 K [17]. We note that our result is much closer to the experimental value than the previously reported calculated value of 573 S/cm [17], which may be due to different calculation methods. These include the choice of exchange-correlation functional, as well as the size of the k -mesh grid used to calculate AHE and ANE, as we found that particularly large mesh is required to reach a satisfactory convergence. Moreover, AHE and ANE are strongly dependent on the Fermi level—a small discrepancy in the position of the Fermi level between the theory and experiment (e.g., through strain, doping, finite size etc.), can result in large changes to the measured/calculated AHE and ANE. The previous authors suggested the discrepancy between the calculated and measured σ_{xy}^A was due to their samples being contaminated by a type- A magnetic structure (which has negative σ_{xy}^A according to their calculation results), resulting in an overall decrease. This same study also examined the

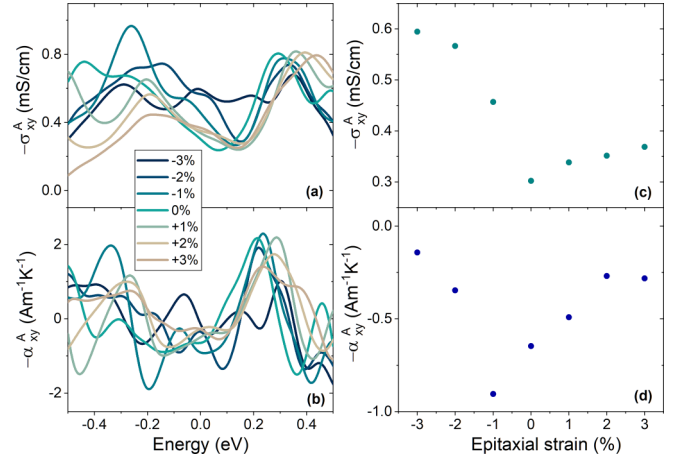


FIG. 2. Calculated anomalous Hall coefficient σ_{xy}^A (a) and anomalous Nernst coefficient α_{xy}^A (b), as a function of a total energy with respect to the Fermi energy under different epitaxial strain at 300 K. Panels (c) and (d) shows the corresponding σ_{xy}^A and α_{xy}^A at the Fermi level as a function of the applied epitaxial strain.

possibility of an extrinsic mechanism accounting for the measured AHE response, leading to the conclusion that the observed AHE is mainly of intrinsic origin.

We next turn to the discussion of the ANE, where we find the calculated ANC, α_{xy}^A , to be 0.65 Am⁻¹ K⁻¹ at the Fermi level for 300 K where experiments report a value of 0.21 Am⁻¹ K⁻¹ at 300 K [17]. Similar to the calculated AHC, we find our calculated ANC value to be three times greater in magnitude than that measured in experiments. We find that the ANC takes its maximum of 0.7 Am⁻¹ K⁻¹ at around 400 K, which is comparable to other promising high-temperature ANE materials such as $\text{UCo}_{0.8}\text{Ru}_{0.2}\text{Al}$ (15 Am⁻¹ K⁻¹) [47], $\text{Co}_3\text{Sn}_2\text{S}_2$ (10 Am⁻¹ K⁻¹) [48], Co_2MnGa (4 Am⁻¹ K⁻¹) [49], Fe_3Sn (2.5 Am⁻¹ K⁻¹) [20], SrRuO_3 (0.6 Am⁻¹ K⁻¹) [50], and Mn_3Sn (0.3 Am⁻¹ K⁻¹) [51]. Thus, Mn_4N can be a promising candidate for thermoelectric applications with its high Néel temperature, small saturation magnetization, and perpendicular magnetic anisotropy.

IV. ENHANCING THE TOPOLOGICAL RESPONSES

To explore routes to enhance the AHC and ANE, and to shed light on measurements of thin films, we calculate how epitaxial strain affects the AHE and ANE in Mn_4N [52]. We first report the calculated σ_{xy}^A and α_{xy}^A for both tensile and compressive strain in Figs. 2(a) and 2(b) at 300 K, respectively. We find that the calculated values of the AHC and ANC at the Fermi level change significantly under epitaxial strain. We predict that both compressive and tensile strains increase the AHC almost linearly away from its turning point, with compressive strain having a much stronger effect [see Fig. 2(c)]. For example, compressive strain increases σ_{xy}^A from -302 S/cm (bulk) to -594 S/cm at -3% , but tensile strain increases σ_{xy}^A to only -369 S/cm at $+3\%$. However, we notice a change in the linear dependence of AHE with strain for -3% , which shows a leveling off compared to smaller strains. Such results hint toward a change in Berry curvature distribution as the AHE is directly related to the Berry curvature as

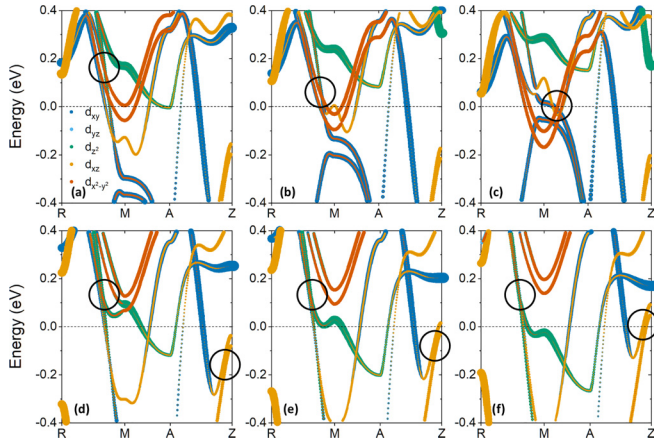


FIG. 3. Calculated band structures with Mn- d orbitals projected as fat bands for epitaxial strains of -1% (a), -2% (b), -3% (c), $+1\%$ (d), $+2\%$ (e), and $+3\%$ (f), respectively. Spin-orbit coupling is included in all calculations with the Fermi level (dotted line) set to 0 eV. Black circles indicate the band-crossings that are the source of Berry curvature.

shown in Eq. (1), which we explore further below. In contrast to the enhancement of AHE with strain, we find the ANE decreases except for a compressive strain of 1% , where we predict α_{xy}^A to be enhanced to a value of $0.9 \text{ Am}^{-1} \text{ K}^{-1}$ from its bulk value of $0.65 \text{ Am}^{-1} \text{ K}^{-1}$ [see Fig. 2(d)]. This is reasonable since α_{xy}^A is approximately proportional to $-\text{d}\sigma_{xy}^A/\text{d}E$ at low temperatures [see Eqs. (1) and (2)].

To understand the intrinsic origins of the enhancement of AHE, and to explain the effect of epitaxial strain on the AHE and ANE, we next inspect our calculated electronic band structure for sources of Berry curvature and how they evolve with strain (Figs. 3 and 4). On plotting the orbital-projected bands for the dominant Mn- d orbitals in Fig. 3, we find that the changes in AHE and ANE can be explained by the creation and movement of Weyl points near BZ edges. Firstly, in the compressive strain region, we find that the band crossings that were responsible for the largest contribution to the AHE in the bulk case are systematically shifted closer to the Fermi level, from $\sim +0.3$ eV in the unstrained case (Fig. 1) to $\sim +0.15$ eV

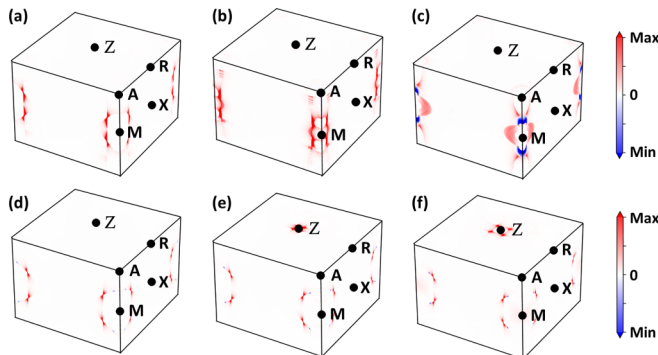


FIG. 4. Berry curvature Ω_z distribution in the BZ for epitaxial strain values of -1% (a), -2% (b), -3% (c), $+1\%$ (d), $+2\%$ (e), and $+3\%$ (f), respectively. Note that only intense Berry curvature distributions are shown and black circles represent the high-symmetry k points in the BZ.

(-1% strain), $\sim +0.05$ eV (-2% strain), and at the Fermi level (-3% strain). This shift in the band crossings is due to both the shift of the Fermi level, and the change in orbital overlap with strain, primarily the relative downwards shift of the $d_{x^2-y^2}$ orbitals, and upwards shifts of the d_{xy} and d_{xz}/d_{yz} orbitals. Closer inspection of the atom- and orbital-projections of these bands reveals that these overlapping bands are comprised mainly of the $d_{x^2-y^2}$, d_{xy} , d_{xz} and d_{yz} orbitals of Mn III (see Fig. S2 within the Supplemental Material [32] for atom-projected bands). The Mn III atoms form a square lattice in the Mn_4N structure: compressive strain greatly increases the orbital overlap of the in-plane orbitals ($d_{x^2-y^2}$ and d_{xy}), resulting in additional crossings in the M-A direction. We also find a slight increase in the overlap between those orbitals with an out-of-plane component (d_{xz} and d_{yz}) due to the competition between the in-plane compression and out-of-plane expansion of those orbitals with compressive strain. Illustrations depicting these changes are shown in Fig. S3 within the Supplemental Material [32]. We find the movement of our band crossings towards the Fermi level with strain to be consistent with our calculated Berry curvature Ω_z , which intensifies with increasing strain, as expected. Crucially, we also find new regions of high Ω_z , which appear at -3% strain [Figs. 3(c) and 4(c)], corresponding to the additional band crossings resulting from the increased overlap of the in-plane orbitals. At -3% , Ω_z has both positive and negative values, which hints toward the formation/creation of a new WP in addition to the WPs at lower compressive strains. The new WP is identified to originate from a new band crossing along the M-A line (see Fig. S1 within the Supplemental Material [32]), which is indicated in Fig. 3(c) and a negative Ω_z distribution can be seen along the M-A line in Fig. 4(c). Thus, with the formation of this new WP, the linear enhancement of AHE gets disrupted when going from -2% to -3% as seen in Fig. 2(c).

On the other hand, in the tensile strain region, we also find band crossings shifting due to both the change in the Fermi level and orbital overlap under the tensile strain. In contrast to compressive strain, bands with $d_{x^2-y^2}$ orbital character shift upwards and bands with the d_{z^2} and d_{xz}/d_{yz} orbital character shift downwards. However, this downward shift of bands with d_{xz}/d_{yz} orbital character is reversed near the high-symmetry point Z, which can be understood from the increased overlap of d_{xz} and d_{yz} orbitals with tensile strain. As a result, another band crossing that was below the Fermi level for the bulk case gets pushed up to the Fermi level, leading to the enhancement of AHE seen in Fig. 2(c). This can also be seen from our calculated Berry curvature Ω_z plots in Figs. 4(d)–4(f) where one can find new regions with high Ω_z between high-symmetry points A and Z that intensifies as more strain is applied.

V. SUMMARY

In summary, we investigated the connection between the Berry curvature and the anomalous Hall and Nernst effects in the antiperovskite ferrimagnet Mn_4N with *ab-initio*-based calculations for bulk and strained cases. A significant Berry curvature originating from WPs was found at the edge of the BZ. Epitaxial strain, both compressive and tensile, is predicted to enhance AHE; however, it is found to generally

decrease ANE, except for the -1% , for all studied strains. At a compressive strain of -3% , new WPs are predicted to form originating from new band crossings induced by orbital overlap. Overall, our results show that enhancement of AHE is due to two factors (i) shifting of the relative Fermi level closer to band crossings, and (ii) the creation of new band crossings with changes of orbital overlap under strain. When taken in conjunction with previous papers on real-space topology [27], such predictions thus indicate that Mn_4N is topological in both real and reciprocal spaces, and could provide an interesting system to explore the interplay of robust topological features in such doubly topological magnetic systems [53]. Furthermore, a large enhancement of AHE with compressive strain may improve the stability of the metastable phases in real space since the topological Hall effect relation to AHE is reported to increase as temperature lowers [18] and topological metastable phases were predicted at low temperatures [27]. We hope our prediction will motivate experimental studies on Mn_4N thin films and

confirm our findings of epitaxial strain effect on AHE and ANE, and will be put to use to design novel devices.

ACKNOWLEDGMENTS

This work is supported by the U.S. Department of Energy, Office of Science, Office of Basic Energy Sciences, Materials Sciences and Engineering Division under Contract No. DE-AC02-05-CH11231 within the Nonequilibrium Magnetic Materials Program (MSMAG). Computational resources were provided by the National Energy Research Scientific Computing Center and the Molecular Foundry, DOE Office of Science User Facilities supported by the Office of Science, U.S. Department of Energy under Contract No. DEAC02-05CH11231. The work performed at the Molecular Foundry was supported by the Office of Science, Office of Basic Energy Sciences, of the U.S. Department of Energy under the same contract.

-
- [1] M. Z. Hasan and C. L. Kane, *Rev. Mod. Phys.* **82**, 3045 (2010).
 [2] X. L. Qi and S. C. Zhang, *Rev. Mod. Phys.* **83**, 1057 (2011).
 [3] A. Bansil, H. Lin, and T. Das, *Rev. Mod. Phys.* **88**, 021004 (2016).
 [4] K. Manna, Y. Sun, L. Muechler, J. Kübler, and C. Felser, *Nat. Rev. Mater.* **3**, 244 (2018).
 [5] D. Xiao, M. C. Chang, and Q. Niu, *Rev. Mod. Phys.* **82**, 1959 (2010).
 [6] N. Nagaosa, J. Sinova, S. Onoda, A. H. MacDonald, and N. P. Ong, *Rev. Mod. Phys.* **82**, 1539 (2010).
 [7] S. Nakagawa and M. Naoe, *J. Appl. Phys.* **75**, 6568 (1994).
 [8] K. M. Ching, W. D. Chang, T. S. Chin, J. G. Duh, and H. C. Ku, *J. Appl. Phys.* **76**, 6582 (1994).
 [9] Y. Yasutomi, K. Ito, T. Sanai, K. Toko, and T. Suemasu, *J. Appl. Phys.* **115**, 17A935 (2014).
 [10] K. Kabara and M. Tsunoda, *J. Appl. Phys.* **117**, 17B512 (2015).
 [11] S. Isogami, K. Masuda, and Y. Miura, *Phys. Rev. Mater.* **4**, 014406 (2020).
 [12] W. J. Takei, G. Shirane, and B. C. Frazer, *Phys. Rev.* **119**, 122 (1960).
 [13] W. J. Takei, R. R. Heikes, and G. Shirane, *Phys. Rev.* **125**, 1893 (1962).
 [14] T. Gushi, M. Jovičević Klug, J. Peña Garcia, S. Ghosh, J. P. Attané, H. Okuno, O. Fruchart, J. Vogel, T. Suemasu, S. Pizzini *et al.*, *Nano Lett.* **19**, 8716 (2019).
 [15] S. Ghosh, T. Komori, A. Hallal, J. Peña Garcia, T. Gushi, T. Hirose, H. Mitarai, H. Okuno, J. Vogel, M. Chshiev *et al.*, *Nano Lett.* **21**, 2580 (2021).
 [16] S. Isogami, N. Rajamanickam, Y. Kozuka, and Y. K. Takahashi, *AIP Adv.* **11**, 105314 (2021).
 [17] S. Isogami, K. Masuda, Y. Miura, N. Rajamanickam, and Y. Sakuraba, *Appl. Phys. Lett.* **118**, 092407 (2021).
 [18] S. Isogami, M. Ohtake, and Y. K. Takahashi, *J. Appl. Phys.* **131**, 073904 (2022).
 [19] S. Isogami, M. Ohtake, Y. Kozuka, and Y. K. Takahashi, *J. Magn. Magn. Mater.* **560**, 169642 (2022).
 [20] Z. Chen, X. Shi, X. Liu, X. Chen, Z. Zhang, and W. Mi, *J. Appl. Phys.* **132**, 233906 (2022).
 [21] Z. Zhang, Q. Zhang, and W. Mi, *Chin. Phys. B* **31**, 047305 (2022).
 [22] Z. Y. Zhang, J. W. Jiang, X. H. Shi, X. Liu, X. Chen, Z. P. Hou, and W. B. Mi, *Rare Met.* **42**, 591 (2023).
 [23] T. Komori, T. Gushi, A. Anzai, L. Vila, J. P. Attané, S. Pizzini, J. Vogel, S. Isogami, K. Toko, and T. Suemasu, *J. Appl. Phys.* **125**, 213902 (2019).
 [24] K. Kabara, M. Tsunoda, and S. Kokado, *AIP Adv.* **7**, 056416 (2017).
 [25] C. T. Ma, T. Q. Hartnett, W. Zhou, P. V. Balachandran, and S. J. Poon, *Appl. Phys. Lett.* **119**, 192406 (2021).
 [26] Q. Wang, Y. Xu, R. Lou, Z. Liu, M. Li, Y. Huang, D. Shen, H. Weng, S. Wang, and H. Lei, *Nat. Commun.* **9**, 3681 (2018).
 [27] T. Bayarara, C. Xu, and L. Bellaïche, *Phys. Rev. Lett.* **127**, 217204 (2021).
 [28] X. Shen, A. Chikamatsu, K. Shigematsu, Y. Hirose, T. Fukumura, and T. Hasegawa, *Appl. Phys. Lett.* **105**, 072410 (2014).
 [29] R. Karplus and J. M. Luttinger, *Phys. Rev.* **95**, 1154 (1954).
 [30] L. Berger, *Phys. Rev. B* **2**, 4559 (1970).
 [31] K. Ito, Y. Yasutomi, K. Kabara, T. Gushi, S. Higashikozono, K. Toko, M. Tsunoda, and T. Suemasu, *AIP Adv.* **6**, 056201 (2016).
 [32] See Supplemental Material at <http://link.aps.org/supplemental/10.1103/PhysRevB.109.014430> for more information on the identified Weyl points in the Brillouin zone for the bulk and the compressive strain of -3% cases and in-depth understanding of the change in orbital projections on the band-structures and their overlap under compressive strain. Furthermore, the effect of different magnetic configurations on the electronic and topological properties is discussed for both Type-A and Type-B types.
 [33] R. Zhang, Y. He, D. Fruchart, J. Coey, and Z. Gercsi, *Acta Mater.* **234**, 118021 (2022).
 [34] Y. He, S. Lenne, Z. Gercsi, G. Atcheson, J. O'Brien, D. Fruchart, K. Rode, and J. M. D. Coey, *Phys. Rev. B* **106**, L060409 (2022).
 [35] G. Kresse and D. Joubert, *Phys. Rev. B* **59**, 1758 (1999).
 [36] P. E. Blöchl, *Phys. Rev. B* **50**, 17953 (1994).

- [37] A. I. Liechtenstein, V. I. Anisimov, and J. Zaanen, *Phys. Rev. B* **52**, R5467 (1995).
- [38] J. P. Perdew, K. Burke, and M. Ernzerhof, *Phys. Rev. Lett.* **77**, 3865 (1996).
- [39] G. Pizzi, V. Vitale, R. Arita, S. Blügel, F. Freimuth, G. Géranton, M. Gibertini, D. Gresch, C. Johnson, T. Koretsune *et al.*, *J. Phys.: Condens. Matter* **32**, 165902 (2020).
- [40] D. Xiao, Y. Yao, Z. Fang, and Q. Niu, *Phys. Rev. Lett.* **97**, 026603 (2006).
- [41] Q. S. Wu, S. N. Zhang, H. F. Song, M. Troyer, and A. A. Soluyanov, *Comput. Phys. Commun.* **224**, 405 (2018).
- [42] H. T. Stokes and D. M. Hatch, *J. Appl. Cryst.* **38**, 237 (2005).
- [43] T. Komori, T. Hirose, T. Gushi, K. Toko, Í. Hanashima, L. Vila, J.-P. Attané, K. Amemiya, and T. Suemasu, *J. Appl. Phys.* **127**, 043903 (2020).
- [44] T. Komori, H. Mitarai, T. Yasuda, S. Ghosh, L. Vila, J. P. Attané, S. Honda, and T. Suemasu, *J. Appl. Phys.* **132**, 143902 (2022).
- [45] T. Komori, T. Horiuchi, H. Mitarai, T. Yasuda, K. Amemiya, and T. Suemasu, *J. Magn. Magn. Mater.* **564**, 170050 (2022).
- [46] H. Mitarai, T. Komori, T. Hirose, K. Ito, S. Ghosh, S. Honda, K. Toko, L. Vila, J.-P. Attané, K. Amemiya, and T. Suemasu, *Phys. Rev. Mater.* **4**, 094401 (2020).
- [47] T. Asaba, V. Ivanov, S. M. Thomas, S. Y. Savrasov, J. D. Thompson, E. D. Bauer, and F. Ronning, *Sci. Adv.* **7**, eabf1467 (2021).
- [48] H. Yang, W. You, J. Wang, J. Huang, C. Xi, X. Xu, C. Cao, M. Tian, Z. A. Xu, J. Dai, and Y. Li, *Phys. Rev. Mater.* **4**, 024202 (2020).
- [49] A. Sakai, Y. P. Mizuta, A. A. Nugroho, R. Sihombing, T. Koretsune, M. T. Suzuki, N. Takemori, R. Ishii, D. Nishio-Hamane, R. Arita *et al.*, *Nat. Phys.* **14**, 1119 (2018).
- [50] T. Miyasato, N. Abe, T. Fujii, A. Asamitsu, S. Onoda, Y. Onose, N. Nagaosa, and Y. Tokura, *Phys. Rev. Lett.* **99**, 086602 (2007).
- [51] M. Ikhlas, T. Tomita, T. Koretsune, M. T. Suzuki, D. Nishio-Hamane, R. Arita, Y. Otani, and S. Nakatsuji, *Nat. Phys.* **13**, 1085 (2017).
- [52] V. Ivanov, E. Banyas, and L. Z. Tan, [arXiv:2211.07773](https://arxiv.org/abs/2211.07773).
- [53] S. F. Weber, S. M. Griffin, and J. B. Neaton, *Phys. Rev. Mater.* **3**, 064206 (2019).